Transition in ICF Capsule Implosions

Grinstein, Fernando
Chiravalle, Vincent P.
Haines, Brian Michael
Greene, Robert Kenneth
Soares Pereira, Filipe Miguel

To be published in: Flow, Turbulence and Combustion

DOI to publisher's version: 10.1007/s10494-024-00607-6

Flow, Turbulence and Combustion
https://doi.org/10.1007/s10494-024-00607-6

RESEARCH

Transition in ICF Capsule Implosions

Fernando F. Grinstein[1] · Vincent P. Chiravalle[1] · Brian M. Haines[1] · Robert K. Greene[1] · Filipe S. Pereira[1]

Received: 10 July 2024 / Accepted: 28 October 2024

Abstract
Longstanding design and reproducibility challenges in inertial confinement fusion (ICF) capsule implosion experiments involve recognizing the need for appropriately characterized and modeled three-dimensional initial conditions and high-fidelity simulation capabilities to predict transitional flow approaching turbulence, material mixing characteristics, and late-time quantities of interest—e.g., fusion yield. We build on previous coarse graining simulations of the indirect-drive national ignition facility (NIF) cryogenic capsule N170601 experiment-a precursor of N221205 which resulted in net energy gain. We apply effectively combined initialization aspects and multiphysics coupling in conjunction with newly available hydrodynamics simulation methods, including directional unsplit algorithms and low Mach-number correction-key advances enabling high fidelity coarse grained simulations of radiation-hydrodynamics driven transition. Our presentation includes discussion of the capsule initialization and implosion dynamics, analysis of the vorticity production budget, transition signatures, quantities of interest—late-time ion temperature and fusion-neutron yield, numerical uncertainty quantification, and comparisons with NIF data.

Keywords ICF capsules · Transition to turbulence · Coarse grained simulations

✉ Fernando F. Grinstein
fgrinstein@lanl.gov

Vincent P. Chiravalle
chiravle@lanl.gov

Brian M. Haines
bmhaines@lanl.gov

Robert K. Greene
greene@lanl.gov

Filipe S. Pereira
fspereira@lanl.gov

[1] X-Computational Physics Division, Los Alamos National Laboratory, P.O. Box 1663, Los Alamos, NM 87545, USA

1 Introduction

The ICF strategy seeks to achieve energy gain through the laser- or X-ray-driven compression of capsules filled with deuterium and tritium (DT, Nuckolls et al. 1972). Recent NIF implosions, which employ the hot spot ignition concept (Lindl 1995) in an indirectly-driven (X-ray-driven) configuration, have demonstrated the feasibility of this concept by producing net energy gain (Abu-Shawareb et al. 2022) with the N221205 shot. Capsules absorb drive energy and ablate mass, causing a rocket-like implosion. In the hot-spot ignition concept, a low-density central core of DT is compressed to high density and pressure to form a"hot spot", which undergoes DT fusion reactions and propagates thermonuclear (TN) burn into a surrounding high-density DT fuel layer that is initially cryogenic DT ice. Success of this approach requires having low entropy in the high-density DT layer, which in turn relies on careful shock timing (Robey et al. 2012, 2013) (shocks form at the ablation front whenever the drive energy increases) and maintaining a high degree of symmetry during the implosion (Haines et al. 2022).

Capsule implosions are classically hydrodynamic unstable at the interfaces between capsule layers (Zhou 2017a, b). In addition to interfaces between the surrounding vacuum, the high-density carbon (HDC) shell, and the DT layers, indirect-drive capsules employ a W-doped layer to isolate the DT fuel layer from X-ray radiation that could pre-heat it and thereby increase its entropy during the course of the implosion. This introduces four interfaces where potentially damaging Richtmyer-Meshkov (RM) instabilities occur; the outside interface is also Rayleigh-Taylor (RT) unstable during shell acceleration. Dominating effects of the flow instabilities can be captured with coarse graining (CG) modeling based on the primary conservation equations and effectively codesigned physics and algorithms (Grinstein 2016). Coarse graining strategies include classical large-eddy simulation (LES) – (Sagaut 2006), focusing on explicit use of subgrid scale (SGS) closure models, and implicit LES (ILES) – (Grinstein et al. 2010, 2023), relying on SGS modeling and filtering provided by physics capturing numerical algorithms.

While the mixing at these interfaces is unlikely to pollute the hot spot (Hammel et al. 2010; Clark et al. 2011), carbon mixed into the fuel layer has the potential to impact its compressibility (Cheng et al. 2016; Clark et al. 2019; Amendt 2021). Furthermore, defects on capsule interfaces, as well as voids, microstructure, and high-Z inclusions can lead to tiny jets (Pickworth et al. 2018; Davidovits et al. 2022; Miller and Goncharov 2022) that can also interrupt compression even when they do not bring contaminant into the hot spot (Haines et al. 2022). On a larger scale, engineering features such as the capsule fill tube (a glass tube used to insert DT into the capsule) and the capsule support tent (a thin formvar membrane used to hold the capsule in place) can seed larger jets that bring contaminant into the hot spot late in the implosion (Clark et al. 2016; Haines et al. 2017, 2017; Weber et al. 2020). Such multi-scale features are particularly challenging to model computationally and rely on complex interactions between hydrodynamics (featuring several hydrodynamic instabilities), radiation, and thermal conduction.

The initial-condition-dependent 3D hydrodynamics of interest in ICF capsule implosions involves transition to turbulence, non-equilibrium turbulence, and late-time relaminarization (Davidovits et al. 2022). Variable density and compressibility add to the complexity of non-equilibrium physics, shocks and other effects to the basic physics associated with material mixing. The time scales over which hydrodynamic instabilities evolve during capsule implosions are generally too short to develop turbulence and remain transitional through explosion (Haines et al. 2014, 2016, 2019). Furthermore, the details of the impacts

of engineering features are highly sensitive to geometric details (see, e.g., Weber et al. 2020; Haines et al. 2020). These combine to produce a highly multi-scale problem that is particularly challenging for CG simulation approaches. The multi-physics aspects also challenge computational resources: radiation typically involves $\gtrsim 70\%$ of computational costs, and state-of-the-art simulations can take years to complete – see (Haines et al. 2020) and (Haines et al. 2020).

1.1 Scope and Plan

Computational and laboratory observations are inherently intrusive due to characterization and modeling uncertainties – *vs.* nature's control of physical phenomena. Suitable modeling, computational design, and initial conditions characterization and parameterization must be combined within appropriate validation and uncertainty quantification frameworks *to ensure repeatability of computational and laboratory experiments for the predictability assessments.* Predictability issues in laboratory/computational collaborative experiments involve characterizing and modeling the relevant physics and conditions within a computational cell *or* instrumentation resolution – SGS level, and at initialization and boundaries – supergrid (SPG) scale. On the other hand, computational simulation strategies also involve uncertainties distinctly associated with the limitations of underlying modeling and numerical paradigms. In practice, the quality of the simulation predictions is limited by insufficently available understanding and characterization of what needs to be modeled in the laboratory experiments and actual computational constraints and costs (rather than choices). NIF shots involve complex physics, SGS and SPG issues: uncertainty bars associated with measured (end result) quantities of interest are often not known.[1]

In what follows, we expand on our early presentation in Grinstein et al. (2023). We build on the *state-of-the-art* CG simulations of the indirect-drive NIF cryogenic capsule N170601 experiment (Clark et al. 2019; Haines et al. 2020) – for which capsule initialization data and previous simulation experience are available. *We seek to address the transitional flow dynamics through bang time using newly available hydrodynamics simulation paradigm advances including directional unsplit algorithms and low Mach-number correction* (Grinstein et al. 2019; Grinstein and Pereira 2021; Pereira et al. 2021; Grinstein et al. 2023) *-potentially enabling high fidelity CG simulations of radiation-hydrodynamics driven transition on coarser grids*.

Our present strategy focuses on predictions for a full capsule quadrant including both poles, based on best available setup conditions; *results on three grid resolutions are used to assess the numerical fidelity of computations for which exact solutions or reference values are unknown*. We apply effectively combined initialization aspects and multiphysics coupling in conjunction with the newly available hydrodynamics simulation methods. We describe the challenging issues of coupling hydrodynamics and multiphysics, capturing transition phenomena, and CG the ICF capsule simulations. This is followed by a discussion of capsule implosion dynamics, capsule initialization, vorticity production budget and transition signatures analysis, evolution of quantities of interest, and numerical uncertainty

[1] It is noteworthy here that the results of the historic N210807 shot in August 7, 2021 breaking the megajoule barrier, could not be repeated over a 16-month period until N221205 in December 5, 2022 – which finally resulted in net energy gain.

quantification analysis. In closing, we present comparisons with available NIF data, summarize our results, and suggest future research directions.

2 Simulations of the N170601 Experiment

Our simulations of ICF capsules utilize the x-Radiation-Adaptive-Grid-Eulerian (xRAGE) radiation hydrodynamics code developed at LANL (Gittings et al. 2008; Haines et al. 2017, 2022). Numerous works have been completed to verify and validate the numerical methods and models within xRAGE, including hydrodynamics, radiation diffusion, 3-temperature (3T) plasma physics, and thermal conduction – see recent survey in Chiravalle (2022).

Unlike prior xRAGE simulations of N170601, which involved either the default directionally split method (Haines et al. 2020) or the directional unsplit method (Chiravalle 2022), in the present study we use the unsplit method together with a low-*Ma* number correction (LMC) algorithm – where *Ma* is the Mach number, which provides an explicit subgrid-scale model allowing for higher fidelity vortex dynamics simulations. Directionally unsplit algorithms are needed when distortions introduced by split schemes are unacceptable, as for incompressible or nearly incompressible flows and magnetohydrodynamic systems where solenoidal conditions must be captured, and for flows involving a high degree of initial symmetry. For example, in ICF spherical capsule implosion simulations Chiravalle (2022) clearly showed spurious 45-degree numerical artifacts and less intense vorticity production introduced with directional-split (*vs.* directional unsplit) xRAGE.

By incorporating the LMC, we additionally address the problem of leading numerical dissipation $\sim 1/Ma$, associated with upwinding in shock-capturing schemes at low *Ma*. The LMC unsplit hydrodynamics can accurately capture the effects of vortex stretching and other basic flow instabilities in the low-*Ma* regimes where mixing physics of interest mostly occurs (Youngs and Williams 2008), resulting in further improved accuracy relative to the default (split) hydrodynamics using less resolution (one-to-two levels coarser) for significant computational cost savings (Grinstein et al. 2019; Grinstein and Pereira 2021; Pereira et al. 2021; Grinstein et al. 2023). We presume miscible interfaces – appropriate for the gas/plasmas (Schmidt number ~ 1) regimes *mostly* involved. The xRAGE directionally unsplit method solves an acoustic Riemann problem based on the Harten-Lax-van Leer-contact (HLLC) approach (Toro et al. 1994).

The relevant formalism including radiation-hydro electron-ion 3T conservation laws in Eulerian form (Mihalas and Mihalas 2013) and their detailed numerical implementation within xRAGE are extensively discussed separately (Chiravalle 2022). The discussion includes choices for opacity and thermal diffusivity models, the method of operator splitting for separating hydrodynamic and diffusive contributions to the governing equations, as well as the numerical technique for updating electron and ion energies due to the electron-ion energy exchange term.

The present 3D simulations used adaptive mesh refinement (AMR) and cubic computational cells, with 0.5 μm, 0.25 μm, and 0.125 μm resolutions-involving between 100 M–3600 M computational cells. Time stepping of the simulations is defined by setting the Courant number to 0.9. Runs were carried out at LANL's *trinity* platform, with number of compute nodes ranging between 100 and 1600. Post-processed quantities of interest used values of species number densities and ion temperatures from the LMC-unsplit xRAGE simulations together with available DT fusion reaction rate data (McNally et al. 1979). Offering such post-processed results amounts to presenting radiation-hydro only

predictions without modeling local exothermicity / energy-deposition effects associated with TN burn reactions.

2.1 Capsule Initialization

Among crucial issues associated with shocked and accelerated material interfaces are sensitivity to initial conditions and their late-time impacts on quantities of interest (Ristorcelli et al. 2013). As noted, accurate characterization and modeling of 3D initial condition drivers in conjunction with high-resolution algorithms are needed to fully understand the interactions of hydrodynamics with complex 3D multiphysics.

The cryogenic ICF capsule in N170601 was described by LePape et al. (2018) and includes an HDC shell that is 70 μm thick with an outer radius of 980 μm (Figure 1). The HDC shell surrounds a cryogenic DT layer with a mass of 0.13 mg. DT gas fills the center of the capsule. The present simulations of N170601 were completed using the same

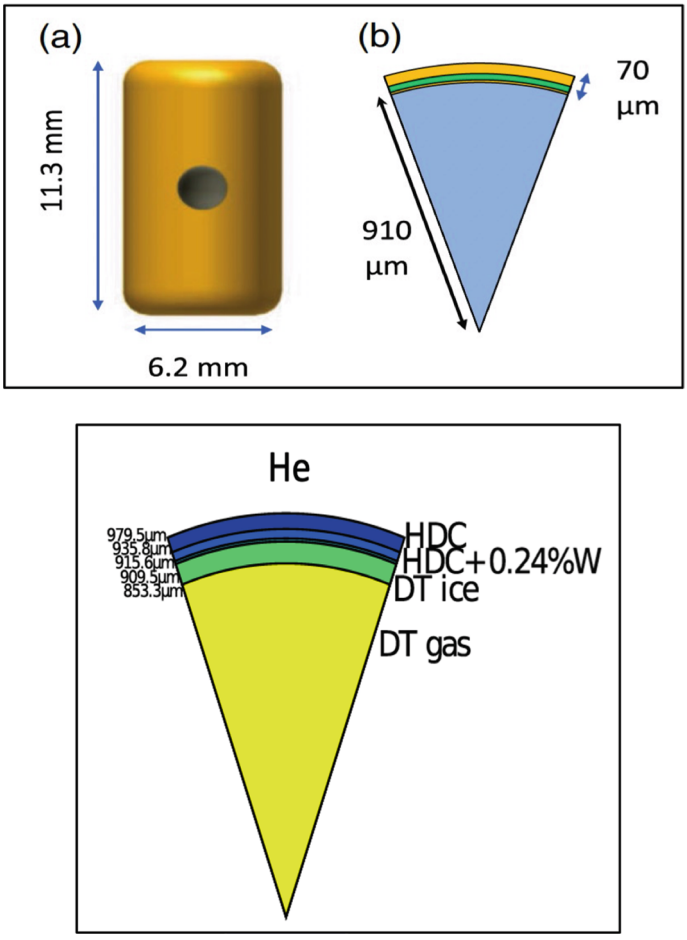

Fig. 1 Schematic of NIF N170601 experiment. Taken from LePape et al. (2018)

2D-linked-into-3D approach as described in the prior work (Chiravalle 2022), where a 2D simulation is mapped onto a spatial domain (quadrant) consisting an 800 μm by 1600 μm by 800 μm sized box region, including both poles of the capsule which are on the y axis and the -y axis, respectively. The x-y and y-z planes are symmetry planes in the 3D simulation. We effectively combine initialization aspects for significant computational cost savings by a) holraum energy fluxes (67 components) at capsule boundary vs. time-based on the previous studies matching data from NIF shots (Clark et al. 2019; Haines et al. 2020) with the HYDRA multiphysics code based on using arbitrary Lagrange Eulerian hydrodynamics (Marinak et al. 2001)—*vs.* presently used xRAGE Eulerian hydrodynamics, b) 2D (67 components) multigroup (MG) radiation-diffusion emulated through effective 2D Gray radiation-diffusion (Haines et al. 2016), c) 2D-to-3D spun for 3D initialization (Haines et al. 2014), and d) radial surface roughness for generic cryogenic capsules (Haan et al. 2011).

The 3D computational methodology begins with a 2D axially symmetric simulation, including MG radiation diffusion with 67 energy groups, representing the energy flux from the hohlraum in the experiment. 2D simulations use MG diffusion to approximate the radiation transport between the hohlraum and the target capsule, utilizing 67 energy flux terms on the computational boundary. These terms were determined by the said separate simulations (Clark et al. 2019; Haines et al. 2020). We used a capsule surface roughness implementation from Chiravalle (2022)—following Haan et al. (2011), with plastic ablator shells replaced with HDC shells, and similar roughness characteristics as for the NIF N170601 capsule (Haines et al. 2020)—except for $\sim 0.5 \mu m$ differences at the poles (Figure 2). The latter differences allow us to gain insights into the effects of a roughness patch in the initial shell conditions – e.g., as associated with the actual presence of the fill tube assembly. The coarsest resolution used in the present studies, 0.5 μm, marginally captures the said roughness differences at poles. Relevant comparisons of quantities of interest for ICF capsule cases with and without surface roughness and with NIF data are presented in section 2.7.

2.2 Coarse Graining

We use LES strategies based on the xRAGE code to revisit the recent simulations (Clark et al. 2019; Haines et al. 2022) of the NIF N170601 ICF capsule experiment. Conceptually, this involves resolving the large scale flow dynamics and using SGS models to address the effects of the unresolved scales.

Implicit LES associated with the directional split xRAGE numerical hydrodynamics has been the default strategy in ICF capsule simulations (Haines et al. 2022) and has also been recently tested with the directional unsplit HLLC algorithm (with no LMC) (Chiravalle 2022). The xRAGE HLLC hydrodynamics provides an optionally added *explicit SGS model* through the LMC—key modeling advance enabling higher fidelity simulations of turbulence (Grinstein et al. 2023). The latter strategy is presently denoted LMC-xRAGE LES.

2.3 Plasma Viscosity Effects

Viscous effects on the Rayleigh--Taylor instability can be found addressed in early work by Menikoff et al. (1978). The idea that viscosity effects would be important only at very short scales in shock-tube problems of interest was suggested by Mikaelian (1993). Plasma viscosity effects on turbulent instability growth were demonstrated by Haines et al. (2014). Plasma

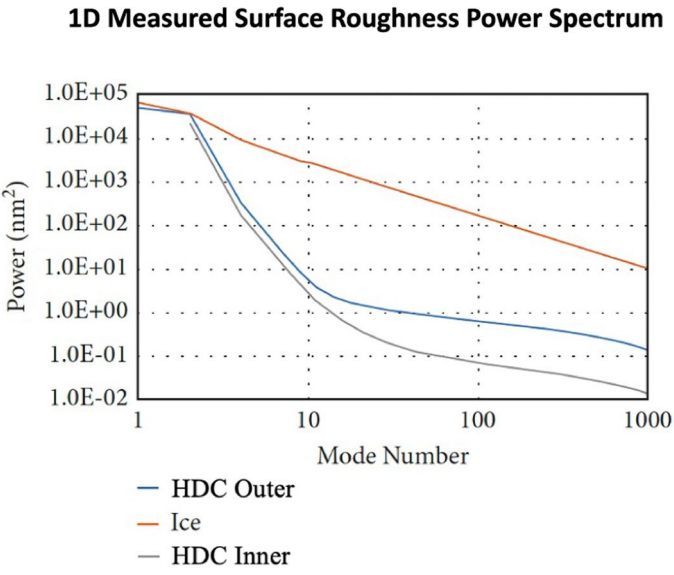

(a)

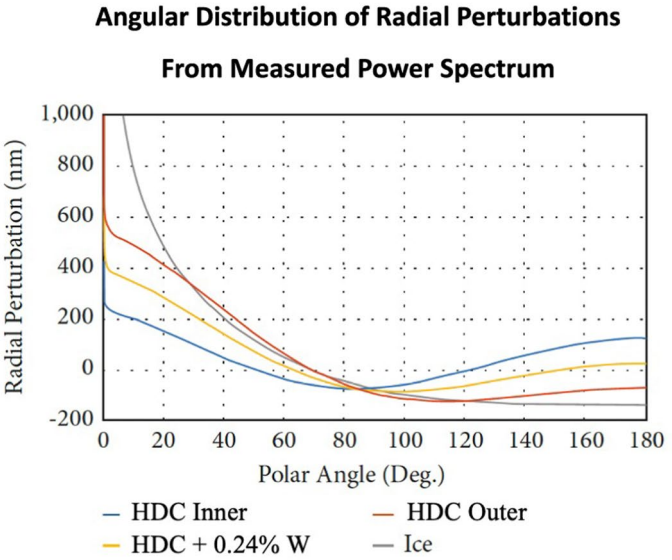

(b)

Fig. 2 Surface roughness features used for for the NIF N170601 simulation, available from Chiravalle (2022) – following Haan et al. (2011)

viscosity effects are expected to grow with temperature as $\sim T^{2.5}$—Molvig et al. (2014) and references therein. Such high temperature viscous effects have been shown to suppress turbulence in the hot spot of ICF capsules at *bang time* (Weber et al. 2014), where the Reynolds

number (Re) was found to be $Re \sim 10 - 100$, quite far from the $Re \sim 10,000$ mixing transition threshold (Dimotakis 2000). Because of their added computational cost, viscous effects have been modeled only for a limited number of ICF capsule experiments—e.g. by Clark et al. (2019).

Plasma viscosity effects depend on the mixture viscosity—volumetrically-weighed blend of material species viscosities. The conventional wisdom supporting the less-expensive (e.g., ~ half-cost) Euler-based capsule simulations such as presently reported is that the mixture viscosity is significantly lower when HDC/DT mixing is present, as typical in the cases of interest. The multi-component molecular viscosity and diffusivity modeling options in the xRAGE code (Molvig et al. 2014; Vold et al. 2017) were not exercised in the presently reported simulations.

2.4 Implosion Dynamics

A shock-interface radius-time diagram based on 1D simulation data, Figure 3, can be used to describe the main events driving the ICF capsule dynamics: shocks forming at the ablation front arrive at the gas region center, bounce outwards, shock and subsequently reshock the interfaces. Early acceleration-based traces depict direct shock propagations as well as more complex ones affected by passage through the HDC/DT interface—e.g., near ~ 5 ns, ~ 6.7 ns.

Postprocessed burn-averaged ion temperature, $T_{burn-avg}$, can be computed based on weighted volumetric average of the ion temperature across the entire mesh based on using available DT fusion reaction rate data at each zone (McNally et al. 1979),

$$T_{burn-avg} = \frac{\int TN_{burn} \cdot T_{ion}\, dV}{\int TN_{burn}\, dV}\,, \tag{1}$$

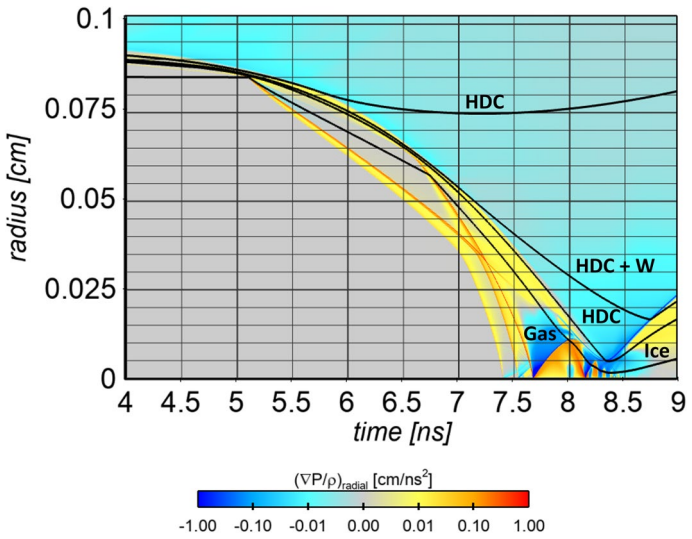

Fig. 3 Evolution of material interface and shock (acceleration based) traces from 1D LMC-unsplit xRAGE simulations of the indirect drive N170601 Experiment at 0.25μm uniform spatial resolution

where TN_{burn} is the TN reaction rate, i.e. the number of fusion neutrons produced in a unit volume per second. Figure 4 indicates three distinct peaks in the burn-averaged ion temperature evolution - based on gas, ice, *or* ice+gas concentration data, with the first one occurring at around 7.5 ns (hot spot), corresponding to when the shocks hit the center of the gas region in the 1D LMC-unsplit xRAGE simulations; double-peak behavior around simulated *bang time* is associated with shock-reshock events at HDC-DT interface discussed above. The latter (1D data based) characteristic temperature curve variation around *bang time* in Figure 4 appear similarly in the gas and ice regions, and also in the 3D context below (Figure 12) – reflecting that it is largely a 1D effect of the implosion dynamics.

The associated evolution of post-processed TN reaction rate is shown in Figure 5. The hot spot forms at the center of the capsule at about 7.7 ns – associated with the shock reaching the capsule center. The time of peak DT fusion reaction rate, *bang time*, occurs at 8.33 ns, near the time for the capsule attaining minimum volume (maximum compressibility)—compared with NIF experiment *bang time* 8.16 ns. Fig. 4 shows slightly higher gas temperatures and most reaction rates happening in the ice. After 8ns, additional peaks are depicted in this burn-averaged ion temperature curve – around peak fusion rate time 8.33 ns, corresponding to reflected shocks from the center hitting the gas/ice interface (and again from new reflections at the center). The burn-averaged ion temperature peaks in Figure 5 and its 3D counterpart—Figure 12 below, correlate closely with multiple interface shock/reshock complex features suggested in the radius-time diagram near *bang time*.

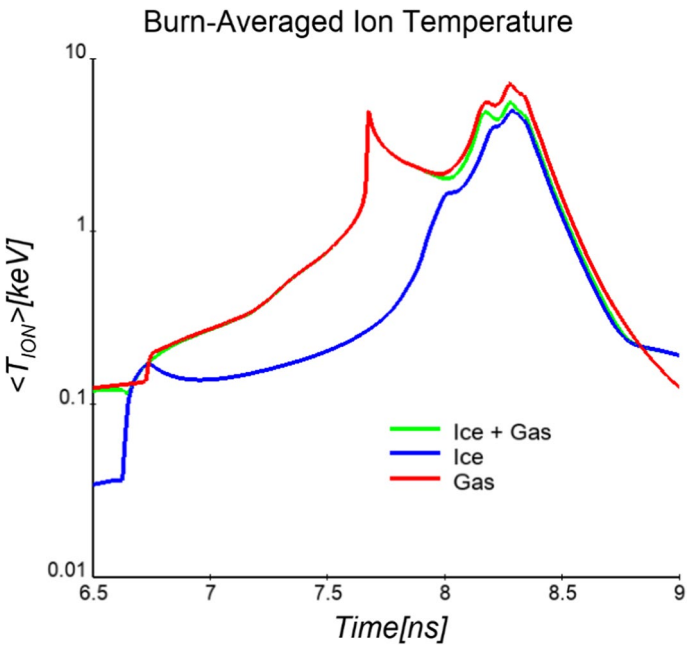

Fig. 4 Evolution of burned-averaged ion temperature – based on gas, ice, and ice+gas concentration data; 1D LMC-unsplit xRAGE simulations

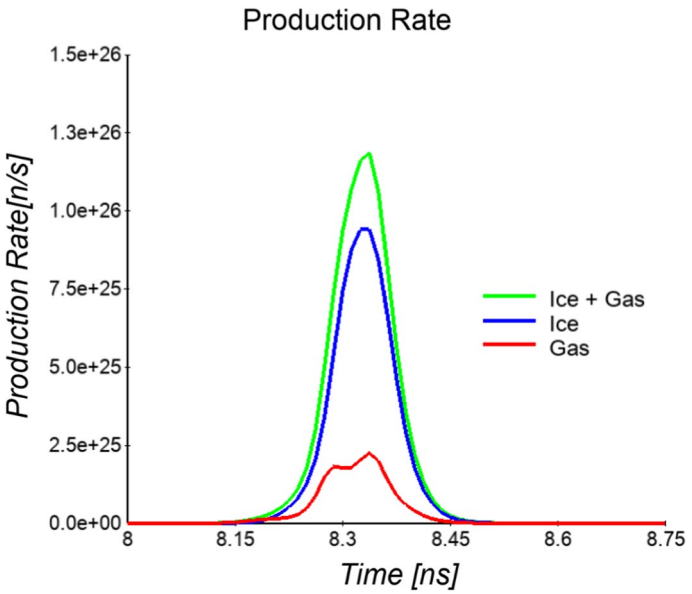

Fig. 5 Evolution of post-processed TN reaction rate – based on gas, ice, and ice+gas concentration data; 1D LMC-unsplit xRAGE simulations

2.5 Transition and Vorticity Dynamics

Transition to turbulence is traditionally viewed in terms of the rapid increase in the energy and the enstrophy production by mode coupling of a spectrum of smaller length scale motions. Transition can lead to an inertial range exhibiting Kolmogorov $-5/3$ wave-number power-law in the turbulence kinetic energy spectrum for sufficiently high Re (Dimotakis 2000; Zhou 2007); there is a very short inertial range when *Re* is just above the mixing transition threshold, $Re \sim 1 - 2 \times 10^4$ based on the integral length scale L (or $Re_\lambda \sim 1 - 1.4 \times 10^2$ based on the Taylor microscale) – Dimotakis (2000). Transition is inherently initial condition dependent (George and Davidson 2004; Ristorcelli et al. 2013; Grinstein 2017).

Figure 6 exhibits (highlighted) high vorticity spots depicting incoming and outgoing jets at zero-degree pole drive DT-Ice-HDC mixing during capsule implosion. The 3D implosion vortex dynamics depicts transitional DT flow through (and after) minimum capsule volume ($\sim$ *bang time*). The promoted generation of non-axisymmetric features associated with 2D-to-3D spun initial surface roughness perturbs at 3D initialization, occurring at 8 ns. Following Figure 3, 2D-to-3D spun time at 8 ns was selected after hot-spot time at about 7.5 ns – when shocks first hit the center of the gas region, and before they rebound onto the HDC shell and before the time of minimum capsule volume around 8.4 ns. Three-D effects are definitely expected to be important by the time of minimum capsule volume.

Vortex ring structures are produced within the (lighter, lower-density) DT gas region. Most vorticity production occurs at the HDC/DT ice interface. Figures 7 indicate that HDC shells do not exhibit significant transition, whereas the opposite is seen on the lighter DT shells. Peak vorticity values are attained around minimum-volume time $\sim 8.2 - 8.4$ ns, and steadily decrease through and after *bang time* between 8.35 ns and 8.7 ns. As noted, ICF capsule implosions are distinct regarding other hydrodynamic instabilities: time scales are short

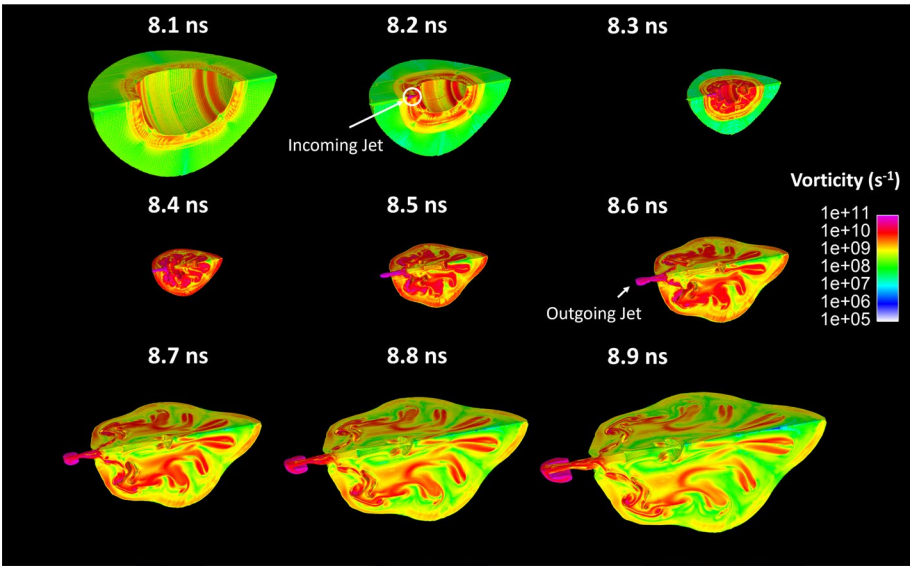

Fig. 6 LMC xRAGE simulations of N170601 experiment; AMR, 0.5μm resolution; DT-Ice colored by vorticity magnitude; 2D-to-3D spun at t=8 ns

relative to turbulence development – fully-developed homogeneous/isotropic turbulence is never achieved – so understanding the 3D transition mechanisms is particularly important.

Figures 6 and 8 show N170601 simulation results through *bang time* for the indirect drive test problem showing the boundaries of the DT gas and inner carbon shell regions, as well as three distinct isosurfaces of λ_2, which help visualize the unstable 3D vortex structures. Vortex tubes are visualized with the λ_2 criterion (Jeong and Hussain 1995), where λ_2 is the second largest eigenvalue of the sum of squares of the symmetrical and anti-symmetrical parts of the velocity gradient tensor.

Transitional vortex ring breakdown is triggered by numerically generated 3D grid-scale (stair-case) fluctuations; the visualizations exhibit features of basic instability mechanisms, including instability and transitional core dynamics of a strained vortex (Pradeep and Hussain 2001) and turbulence cascade pathways driven by self-induced vortex deformations, stretching, and reconnections (Hussain and Husain 1989; Grinstein 1995, 2001; Leweke et al. 2016; Yao and Hussain 2022). For reference, Figure 9 depicts the noted transitional small-scale flow dynamical features for the finest (0.125μm) resolution case.

2.5.1 Enstrophy Production and Transition Signature

Flow instabilities and associated vortex production driving high *Re* mixing are crucial ingredients in the enstrophy budget equation,

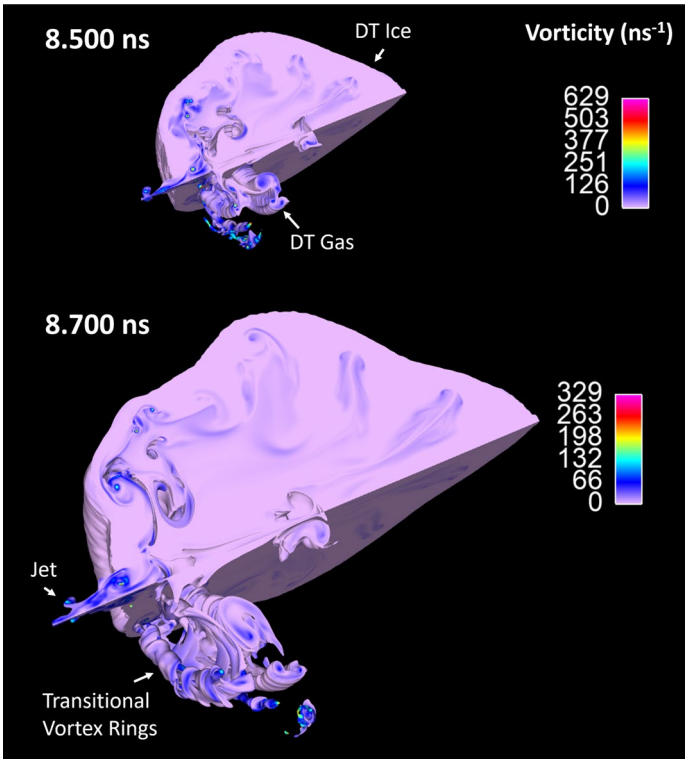

Fig. 7 Snapshots of the capsule implosion 3D vortex dynamics in terms of DT-Ice / DT-Gas colored by vorticity magnitude ω; LMC xRAGE, AMR, 0.25μm resolution, 600 million cells; 2D-to-3D spun @ t=8 ns; NIF *bang-time* 8.16 ns (8.33 ns in simulations); same scale used for both visualizations

$$D\Omega/Dt \sim \underbrace{\{\omega_i s_{ij} \omega_j\}}_{(a)\ Vortex\ Stretching} + \underbrace{\{\omega_i \omega_j\} S_{ij}}_{(b)\ KH,\ Compression,\ BP,...} + \underbrace{\epsilon_{ijk} \overline{\rho}^{-2} \{\omega_i \rho_{,j}\} P_{,k}}_{(c)\ Baroclinic:\ RT,\ RM,\ ...} + \underbrace{\epsilon_{ijk} \overline{\rho}^{-2} \{\omega_j p_{,i}\} \rho_{,k}}_{(d)\ other\ Baroclinic\ ...} + \textit{viscous dissipation terms} \quad , \tag{2}$$

where mean enstrophy $\Omega = \{\omega_i \omega_i\}$, is defined in terms of the vorticity components ω_i, P is mean pressure, s_{ij} and S_{ij} are fluctuating and mean strain rates, $s_{ij} = (u_{i,j} + u_{j,i})/2$, and $\overline{\rho}$ is mean mass density, and the brackets $\{\}$ denote ensemble averaging.

Highlighted terms on the right-hand side of equation 2 depict *inherently inviscid* instability mechanisms governing the high *Re* regimes: (a) vortex stretching driving vortex cascade and transition to turbulence—only present in 3D; (b) mean-shear driven Kelvin-Helmholtz instability, mean compression by shock and the Bell-Plesset convergence instability; (c) two baroclinic instabilities proportional to pressure gradients—*one* corresponding to the classical RM and RT drivers; (d) two other baroclinic instabilities proportional to density gradients.

Figure 11 compares the major enstrophy production contributions for the finest (0.125 μm) resolution, including baroclinic torque, compression, and vortex

stretching—equation 2. The brackets {} in equation 2 are taken to be volumetric integration over a spherical subdomain of radius $0.04cm$—Figure 10. They are added up into a *total* enstrophy production measure. Baroclinic contribution is much less than stretching and compression for the times considered after time ~ 8.2 ns, stretching being the main contribution—signature of transition to turbulence, with the positive stretching contribution depicting the (dominating) forward cascade. Enstrophy production results are qualitatively similar for the coarser resolutions but with reduced actual production—e.g., peak enstrophy production is halved for the 0.25μm resolution case.

In section 2.4, we used a shock-interface radius-time diagram for the 1D implosion history based on simulation data to describe the main events driving the relevant ICF capsule dynamics: shocks forming at the ablation front arrive at the center of the DT gas region around 7.5 ns, bounce outwards, shock and subsequently reshock the interfaces. After 8 ns, reflected shocks from the center hitting the gas/ice interface underlie the first peak in the total enstrophy production noted near *bang time* 8.33 ns in Figure 11. Thereafter, there is a slight total drop around maximum compression (minimum volume) time ~ 8.4 ns, followed by a larger total enstrophy production peak somewhat later (time $\gtrapprox$ 8.45ns) associated with new reflections and new reshocking of the interfaces—suggested in Figure 3.

2.6 Quantities of Interest and Uncertainty Analysis

For the sake of simplified quantitative mix analysis, we can consider an integrated mixing measure between material species 1 and 2 – following Hahn et al. (2011), computed using local raw quantities,

$$MIX_{1,2} = \int \rho^2 \, Y_1 Y_2 \, dV \, , \tag{3}$$

in terms of volumetric integrals involving mass density ρ, and fractions Y_1 and Y_2.

Robust $T_{burn-avg}$ and $MIX_{HDC,DT}$ (nearly resolution independent) predictions are obtained; double-peak temperature around simulated *bang time*, Figure 12, depict shock-reshock HDC-DT interface discussed above in terms of radius-time diagram—Figure 3. Differences apparent upon comparing Figure 12 with its counterpart Figure 4—based on 1D LMC xRAGE simulation results, reflect the unaccounted-for 3D effects.

The mix measure results depict converging $MIX_{DT_{Ice},DT_{Gas}}$ predictions. Peak mix occurs around ~ $8.4ns$, at the time for minimum capsule volume (cf. Figure 6). HDC/DT (heavy/light) mix hydro-driven and very robust(resolution independent); ~ 1/1000 weaker DTice/DTgas mix (than HDC/DT mix) is somewhat grid resolution dependent, but convergent—as 2nd order numerical diffusivity emulates effective physical diffusivity and associated effective Reynolds number and resolved/unresolved scale separation increase with vanishing grid resolution (Grinstein and Wachtor 2016) Fig. 13.

The numerical uncertainty of the DTice/DTgas mix measures, $U_n(\Theta)$ was assessed. This exercise aimed at ascertaining the numerical fidelity of the present computations, for which exact reference solutions are not known. $U_{\mathrm{n}}(\Theta)$ provides an estimate for an interval containing the exact solution of the mathematical model with 95% confidence. Hence, it reduces upon grid refinement, increasing the numerical accuracy of the simulations. In this work, $U_{\mathrm{n}}(\Theta)$ is estimated with the method proposed by Eça and Hoekstra (2014) using the solutions obtained with the three grid resolutions available. Description of the method and concept of numerical uncertainty are given in ASME: Standard (2009) and Eça and Hoekstra (2014) Fig. 14.

Fig. 8 N170601 simulations based on LMC xRAGE, AMR, 0.25μm resolution, 600 M cells; 2D-to-3D spun @ t=8ns (NIF experiment *bang time* 8.16 ns). Visualizations: 1) HDC/DT and DT-ice/DT-gas interfaces, 2) λ_2 vortex criterion

Figure 15 depicts the temporal evolution of the mixing measure of DT-Ice / DT-Gas (equation 3) and the respecting numerical uncertainty (red area), based on LMC-xRAGE LES data for 0.5 μm, 0.25 μm, and 0.125 μm grid resolutions. The analysis estimates values of numerical uncertainty between $\pm 3\%$ and $\pm 8\%$ for DT-Ice / DT-gas mix values near minimum volume. Given the negligible numerical uncertainty involved for the other two—$T_{burn-avg}$ and $MIX_{HDC,DT}$ integrated measures, the 0.125 μm grid resolution thus appears to be adequate to predict the present quantities of interest.

2.7 Comparisons with NIF Data

Tables 1 and 2 compare 1D, 2D, and 3D simulated peak burn-averaged ion temperature near *bang time* and the corresponding total number of neutrons produced from DT fusion reactions—with and without including modeled surface roughness. Quoted NIF data was taken from Table 1 in Clark et al. (2019).

To facilitate comparison with the 3D simulations, the 1D results presented follow a similar computational approach as the 2D and 3D simulations, where MG radiation diffusion is turned off at 8 ns, and Gray diffusion is then used. Using this computational approach, 1D simulations produce about 2.2×10^{16} neutrons from DT fusion reactions, which is considerably more than what was observed in the N170601 experiment. The neutron production is only 1.3×10^{16} in 1D simulations where MG diffusion is active after 8 ns. The peak burn-averaged ion temperature near *bang time* in 1D simulations where Gray radiation diffusion is used after 8 ns is about 5.9 keV, which is 5% higher than in corresponding simulations with MG diffusion (NIF reference value is 4.9 keV). Results do not significantly depend on the presence of roughness.

The 2D and 3D simulations produce a smaller number of neutrons driven by additional mixing at the ice/carbon interface. In 3D, vortex rings at the ice/carbon interface mix material from the carbon shell into the DT ice region, decreasing the overall number of DT fusion reactions. Vorticity production may explain why 3D simulations produce fewer neutrons than corresponding 1D simulations. There is no evidence that transition to turbulence occurs within the DT ice and DT gas regions at 0.5 μ m resolution, for which vortex rings are generated at the ice/carbon interface and remain largely coherent. As noted, however, transition is suggested for the finer resolutions, 0.25 μm and 0.125 μm – for which higher vorticity production also occurs.

The fine resolved 3D xRAGE simulations and NIF experiments agree fairly well on the (post-processed) quantities of interest: simulations underpredict total fusion neutron numbers ~14%, and overpredict the burn-averaged temperature by ~13%; moreover, as noted in section 2.4, *bang time* is slightly overpredicted ~2%. Our simulated burn width is 109 ns, as opposed to the data—165 ns. Our simulated burn-averaged ion temperature is 5.59 keV, as opposed to the data – 4.93 keV. These quantities of interest appear to be mainly end-results driven by 3D radiation hydrodynamics. The 3D unsplit Eulerian hydrodynamic method in xRAGE used for the present study is substantially different than the ALE method utilized in HYDRA by Clark et al. (2019).

The 3D simulations of N170601 with HYDRA in Clark et al. (2019) included a more complete set of physical models such as MG radiation diffusion, plasma viscosity, and

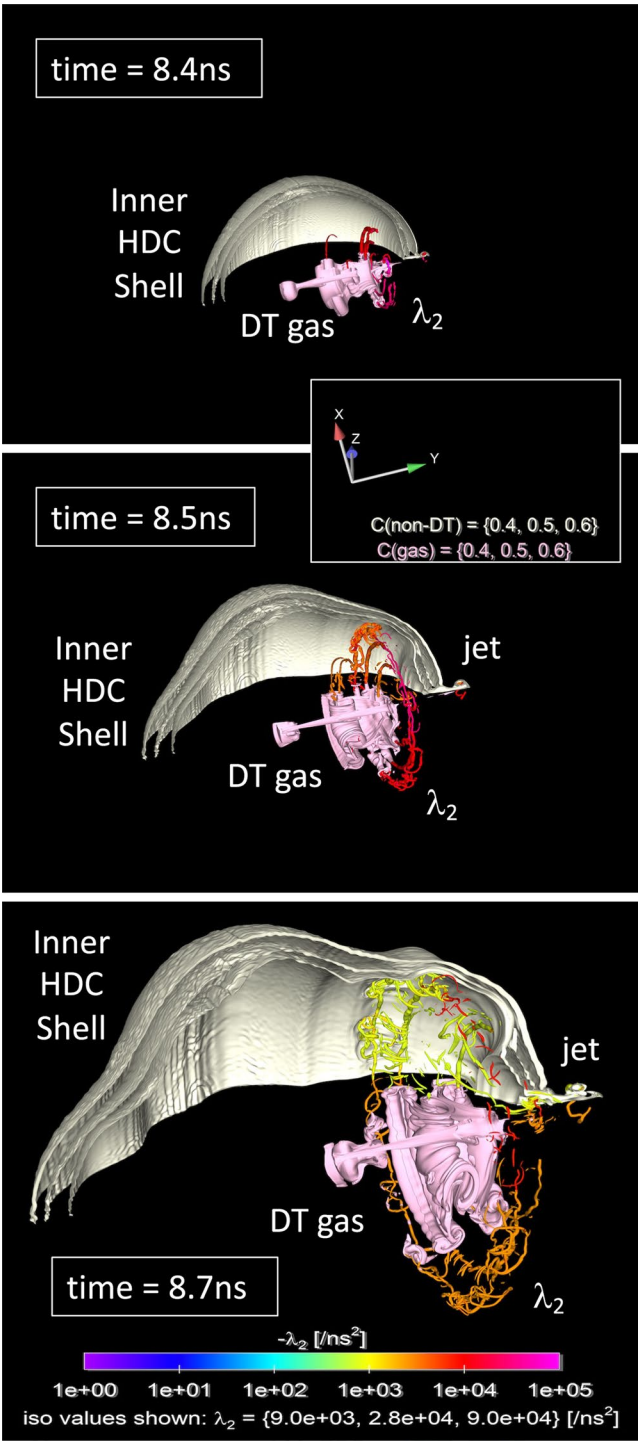
time = 8.4ns
Inner
HDC
Shell
DT gas
λ_2
X
Z
Y
C(non-DT) = {0.4, 0.5, 0.6}
C(gas) = {0.4, 0.5, 0.6}
time = 8.5ns
Inner
HDC
Shell
jet
DT gas
λ_2
Inner
HDC
Shell
jet
DT gas
time = 8.7ns
λ_2
$-\lambda_2$ [/ns^2]
1e+00 1e+01 1e+02 1e+03 1e+04 1e+05
iso values shown: λ_2 = {9.0e+03, 2.8e+04, 9.0e+04} [/ns^2]

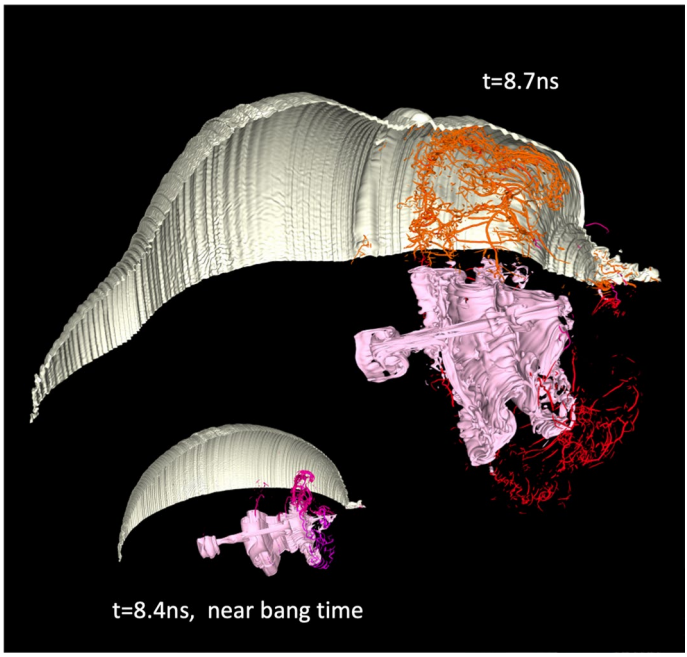

Fig. 9 N170601 simulations based on LMC xRAGE Rad-Hydro, AMR, 0.125 μm resolution, Visualizations at t= 8.4 ns and t= 8.7 ns; 2D-to-3D spun @ t=8ns – for reference: NIF experiment *bang time* 8.16 ns. HDC/DT and DT ice/gas interface visualizations are based on HDC/DT mass fraction (0.6) and DT ice/gas mass fraction (0.5) isosurfaces; as in Figure 8, λ_2 vortex criterion is based on three selected negative λ values

charged particle transport, in particular, which accounts for the deposition within the capsule of the energy released from DT fusion. In addition they explicitly simulate the fill tube and the resulting 3D perturbations to the capsule implosion. With this higher fidelity, they achieve better agreement for the measured bang time, burn width, and ion temperature, relative to our 3D simulations.

We attribute the neutron-yield underprediction in our simulations to two effects: the unaccounted-for plasma viscosity—which would reduce actual vorticity production if present and increase neutron production, as well as our omission of energy deposition within the capsule due to DT fusion, which would also increase neutron production. When we include an energy source term in our 1D simulations to approximate the energy deposition from DT fusion we observe about a 30 % increase in neutron production, relative to our baseline 1D simulations without energy deposition. We expect this to be true for our 3D simulations as well. In addition, the limited results comparing MG *vs.* GRAY 1D predictions in Table 1 suggest that the lack of MG modeling may be a contributing factor to overpredicting burn-averaged temperature in our finest resolved 3D simulations.

Despite the different numerical methods for hydrodynamics, and despite our simulations having lower fidelity physical models including GRAY diffusion without both plasma viscosity and energy deposition from DT fusion, the total neutron production from our 2D simulation and our more highly resolved 3D simulations, presented in Table 2, are in fairly

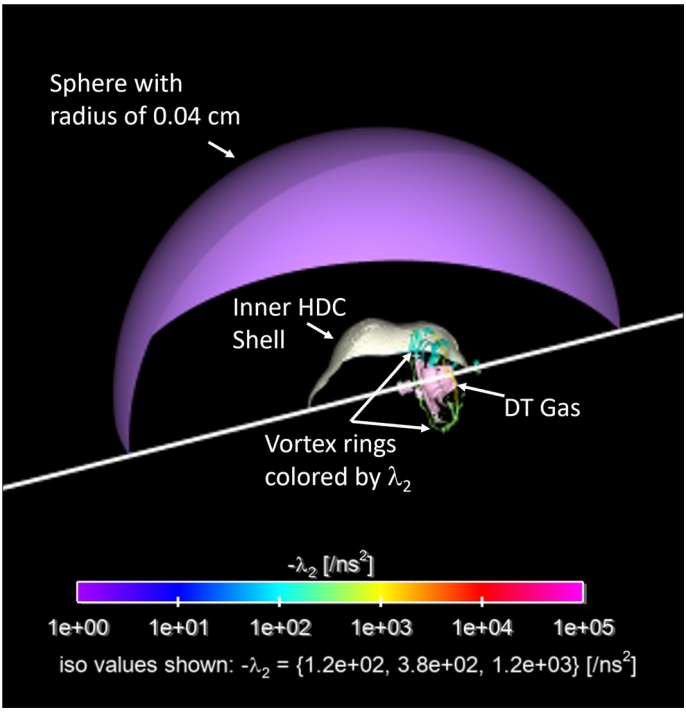

Fig. 10 Spherical subdomain of radius 0.04*cm* used for enstrophy budget analysis. Evenly spaced cells are involved in the subdomain

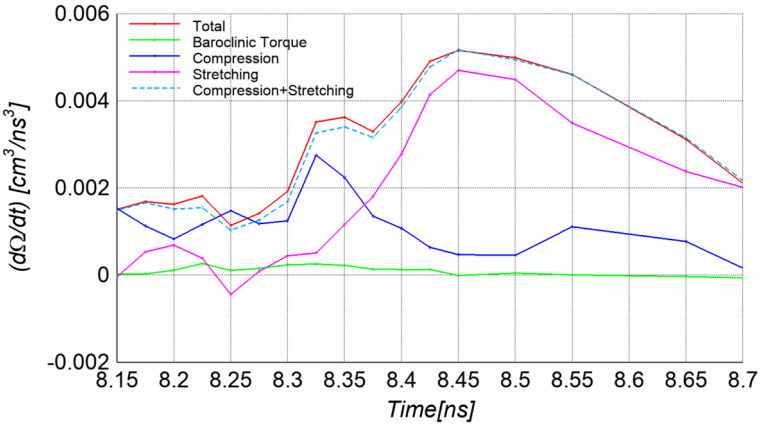

Fig. 11 Enstrophy production based on LMC xRAGE radiation-hydro, AMR, 0.125 μm resolution

good agreement with the corresponding simulation results from Clark et al. (2019). They report a total neutron production of 1.75 $\times 10^{16}$ for their 2D simulation and 1.31 $\times 10^{16}$ for their 3D simulation, as opposed to our values of 1.81 $\times 10^{16}$ and 1.26 $\times 10^{16}$, respectively.

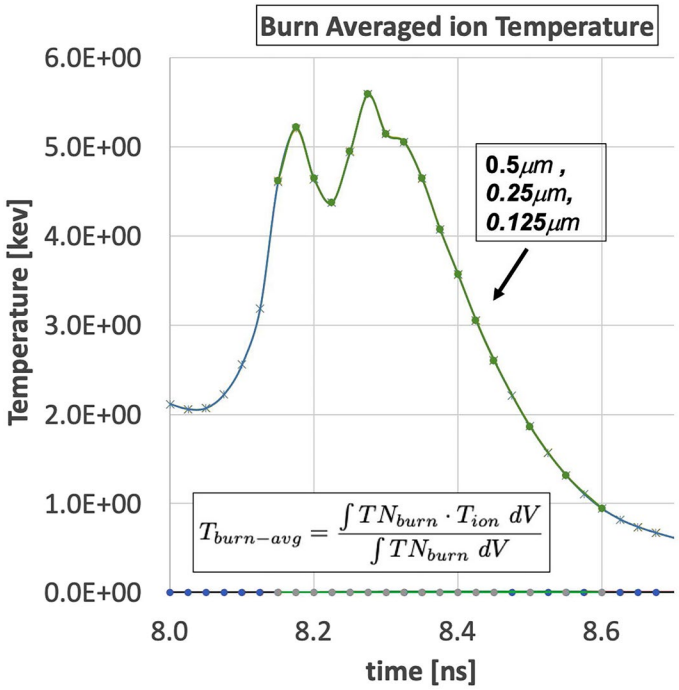

Fig. 12 Evolution of post-processed TN burn averaged T_{ion} – based on equation 1; cf. layout depicting capsule dynamics in Figure 6. Radiation-hydro transition in NIF N170601. LMC-xRAGE LES compared results associated with 0.5 μm, 0.25 μm, and 0.125 μm grid resolutions are indistinguishable; 2D-to-3D spun at t=8 ns. NIF experiment *bang time* 8.16 ns

3 Summary and Outlook

We surveyed challenging ICF capsule issues of coupling hydrodynamics and multiphysics associated with capturing transition phenomena and CG the simulations. We revisited the recent simulations (Clark et al. 2019; Haines et al. 2022) of the NIF N170601 ICF capsule experiment, with the new xRAGE hydrodynamics including directional unsplit HLLC algorithm and LMC explicit subgrid scale model—key modeling advances enabling high fidelity CG simulations of turbulence (Grinstein et al. 2023)—showing the potential of a relevant CG strategy for simulating complex transitional coupled hydrodynamics-multiphysics on coarser grids in the present ICF capsule implosion context.

Initialization aspects effectively combined included a) Holraum energy fluxes (67) at capsule boundary vs. time based on the previous said studies matching data from NIF shots (Clark et al. 2019; Haines et al. 2020), b) 2D (67 component) MG radiation diffusion emulated through effective 2D Gray radiation-diffusion, c) radial surface roughness for generic cryogenic capsules (Haan et al. 2011), and 2D-to-3D spun for 3D initialization. We used a generic capsule surface roughness implementation with similar roughness characteristics as for the NIF N170601 capsule—except for the noted $\sim 0.5\mu m$ differences at the poles. The latter differences usefully provide insights into the effects of a roughness patch in the initial shell conditions.

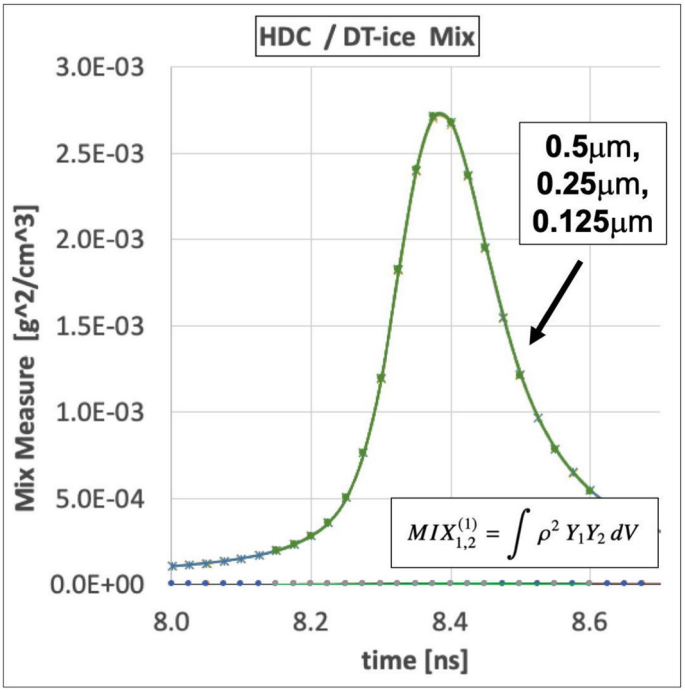

Fig. 13 Evolution of inner-HDC / DT-Ice mixing measures; mix measure involves volumetric integration (no additional averaging) based on equation 3. LMC-xRAGE LES compared results associated with 0.5 μm, 0.25 μm, and 0.125 μm grid resolutions are indistinguishable; 2D-to-3D spun at t=8 ns

We compared 1D, 2D, and 3D simulated peak burn-averaged ion temperature near *bang time* and the corresponding total number of neutrons produced from DT fusion reactions—with and without including modeled surface roughness. Results do not significantly depend on the presence of roughness. Post-processed TN-burn quantities of interest were calculated using values of species number densities and ion temperatures from the LMC-xRAGE LES simulations together with available DT fusion reaction rate data (McNally et al. 1979). As noted, offering such post-processed results amounts to presenting radiation-hydro only predictions without modeling local exothermicity/energy-deposition effects associated with TN burn reactions.

Discussion of the results included capsule initialization and implosion dynamics, analysis of the vorticity production budget, evolution of quantities of interest, uncertainty analysis, transition signatures, and comparisons with NIF data. Baroclinic vorticity production contribution was found to be much less than stretching and compression near *bang time*, stretching being the main contribution as expected for transition to turbulence, with positive stretching contribution depicting (dominating) forward cascade around *bang time*. Robust (nearly resolution independent) $T_{burn-avg}$ and $MIX_{HDC,DT}$ predictions were obtained, exhibiting double-peaked temperature around simulated *bang time*. On the other hand, the $MIX_{DT_{Ice},DT_{Gas}}$ mix measure results depict converging predictions. Peak mix occurs around time for minimum capsule volume. HDC/DT (heavy/light) mix hydro-driven and very robust(resolution independent); $\sim \times 10^{-3}$ weaker DTice/DTgas mix (than HDC/DT mix) is somewhat grid resolution dependent, but

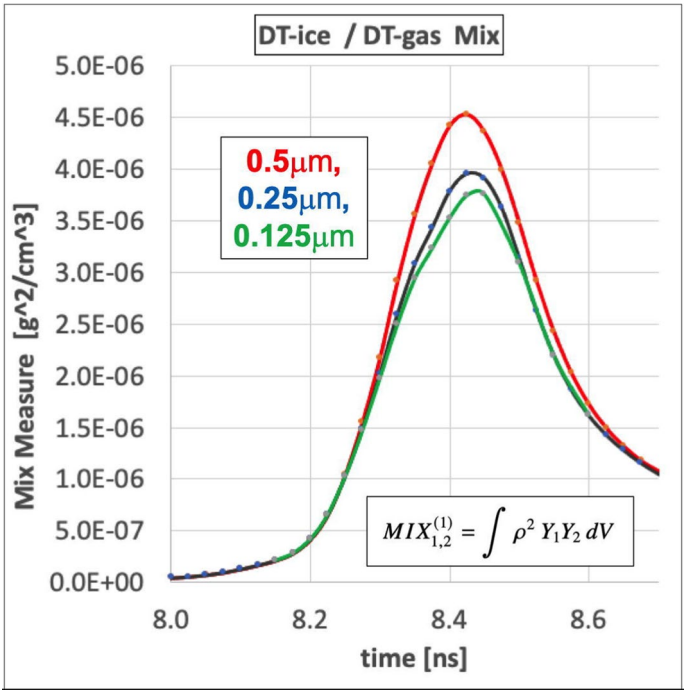

Fig. 14 Evolution of DT-Ice / DT-gas mixing measures; mix measure involves volumetric integration (no additional averaging) based on equation 3. LMC-xRAGE LES results with 0.5 μm, 0.25 μm, and 0.125 μm grid resolution are compared; 2D-to-3D spun at t=8 ns

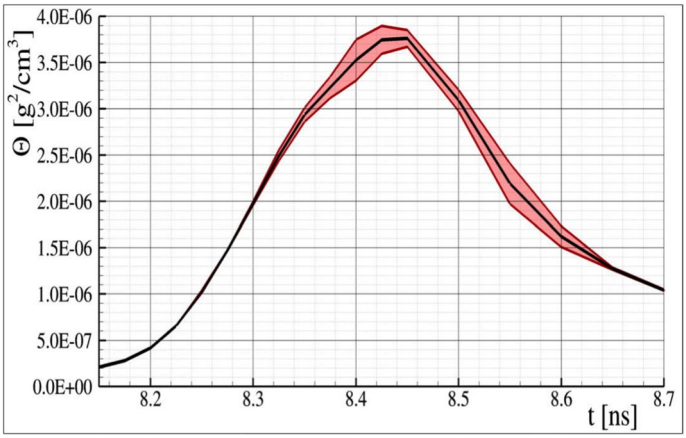

Fig. 15 Numerical uncertainty quantification analysis of the evolution of the DT-Ice / DT-gas mixing measure based on LMC-xRAGE data for 0.5 μm, 0.25 μm, and 0.125 μm grid resolutions

convergent—as 2nd order numerical diffusivity is capable of emulating effective physical diffusivity. Uncertainty analysis was based on LMC-xRAGE LES data for 0.5μm, 0.25μm, and 0.125μm grid resolutions. The analysis estimates numerical uncertainty

Table 1 LMC-xRAGE (no roughness) post-processed TN-Burn Predictions

	$1D^{(MG)}_{0.125\mu m}$	$1D^{(Gray)}_{0.125\mu m}$	$2D^{(nr,Gray)}_{0.5\mu m}$	$3D^{(nr,Gray)}_{0.5\mu m}$	NIF
Burn Average Temperature (keV)	5.6	5.9	5.78	5.75	4.93
DT fusion neutrons ($\times 10^{16}$)	1.3	2.2	1.92	1.92	1.46

Table 2 LMC-xRAGE (with roughness) post-processed TN-Burn Predictions

	$1D^{(Gray)}_{0.125\mu m}$	$2D^{(r,Gray)}_{0.5\mu m}$	$3D^{(r,Gray)}_{0.5\mu m}$	$3D^{(r,Gray)}_{0.25\mu m}$	$3D^{(r,Gray)}_{0.125\mu m}$	NIF
Burn Averaged Temperature (keV)	5.9	5.75	5.58	5.59	5.59	4.93
DT fusion neutrons ($\times 10^{16}$)	2.2	1.81	1.82	1.26	1.26	1.46

values between $\pm 3\%$ and $\pm 8\%$ for DT-Ice / DT-gas mix values near minimum volume. Negligible numerical uncertainty is involved for the other two integrated measures, pointing out the adequacy of the finest grid resolution to predict the present quantities of interest.

The LMC-xRAGE LES CG strategy enabled accurate predictions on relatively coarse grids, providing insights into initial conditions effects on vorticity and mixing dynamics in the N170601 experiment: i) demonstrating outgoing jetting at zero-degree pole driving HDC / DT mix (e.g., associated with surface roughness patch at pole due to fill-tube effects), and, ii) depicting transitional (vortex stretching driven) 3D DT flow dynamics through *bang time*.

Quality of the simulation predictions is limited in practice by insufficiently available understanding and characterization in the laboratory studies of what needs to be modeled—such as TN energy deposition mechanisms to be emulated by charged-particle-transport algorithms. In addition, computational constraints and costs (rather than choice) typically drive what is used: Gray vs. MG radiation-diffusion, and multi-component molecular viscosity and diffusivity xRAGE options not being exercised. Potentially important unresolved (temperature dependent) plasma viscosity and MG radiation effects on the observed transition near *bang time* remain to be assessed in detail. Simulation initialization also deserves further attention: only grid-scale staircase fluctuations were involved in the present simulations, and 2D-to-3D spun initialization may inhibit 3D growth. Exploring the overall effects of promoting breaking of the 2D symmetry by adding 3D perturbs at initialization (Haines et al. 2014) and/or by starting the simulations in fully 3D mode from the beginning, are definitely warranted.

Author Contributions The authors have read the Nature Portfolio journal policies on author responsibilities and submit this manuscript in accordance with those policies. All of the material is owned by the authors and/or no permissions are required. All authors contributed to the text and figures.

Funding LANL is operated by TRIAD National Security, LLC for the US DOE NNSA under contract 89233218CNA000001. This research was supported by the LANL ASC PEM, V&V, and ICF programs.

Data Availibility Statement The authors do not have any research data outside the submitted manuscript file.

Declarations

Conflict of interest The authors have no Conflict of interest as defined by Springer, or other interests that might be perceived to influence the results and/or discussion reported in this paper.

Ethical approval There are no ethical conflicts.

Informed consent The authors confirm reading the journal policies and submit this manuscript in accordance with those policies.

References

Abu-Shawareb, H., Acree, R., Adams, P., Adams, J., Addis, B., Aden, R., Adrian, P., Afeyan, B.B., Aggleton, M., et al.: Lawson criterion for ignition exceeded in an inertial fusion experiment. Phys. Rev. Lett. **129**, 075001 (2022). https://doi.org/10.1103/PhysRevLett.129.075001

Amendt, P.: Entropy generation from hydrodynamic mixing in inertial confinement fusion indirect-drive targets. Phys. Plasmas **28**(7), 072701 (2021). https://doi.org/10.1063/5.0049114

ASME: Standard for verification and validation in computational fluid dynamics and heat transfer—ASME V &V 20-2009. ASME, USA (2009)

Cheng, B., Kwan, T.J.T., Wang, Y.M., Yi, S.A., Batha, S.H., Wysocki, F.J.: Effects of preheat and mix on the fuel adiabat of an imploding capsule. Phys. Plasmas **23**(12), 120702 (2016). https://doi.org/10.1063/1.4971814

Chiravalle, V.P.: Verification and validation of two hydrodynamic methods for simulations of high energy density physics problems. Laser Part. Beams **2022**, 8720064 (2022). https://doi.org/10.1155/2022/8720064

Clark, D.S., Haan, S.W., Cook, A.W., Edwards, M.J., Hammel, B.A., Koning, J.M., Marinak, M.M.: Short-wavelength and three-dimensional instability evolution in national ignition facility ignition capsule designs. Phys. Plasmas **18**(8), 082701 (2011). https://doi.org/10.1063/1.3609834

Clark, D.S., Weber, C.R., Milovich, J.L., Salmonson, J.D., Kritcher, A.L., Haan, S.W., Hammel, B.A., Hinkel, D.E., Hurricane, O.A., Jones, O.S., Marinak, M.M., Patel, P.K., Robey, H.F., Sepke, S.M., Edwards, M.J.: Three-dimensional simulations of low foot and high foot implosion experiments on the national ignition facility. Phys. Plasmas **23**(5), 056302 (2016). https://doi.org/10.1063/1.4943527

Clark, D.S., Weber, C.R., Milovich, J.L., Pak, A.E., Casey, D.T., Hammel, B.A., Ho, D.D., Jones, O.S., Koning, J.M., Kritcher, A.L., Marinak, M.M., Masse, L.P., Munro, D.H., Patel, M.V., Patel, P.K., Robey, H.F., Schroeder, C.R., Sepke, S.M., Edwards, M.J.: Three-dimensional modeling and hydrodynamic scaling of National Ignition Facility implosions. Phys. Plasmas **26** (2019)

Davidovits, S., Weber, C.R., Clark, D.S.: Modeling ablator grain structure impacts in ICF implosions. Phys. Plasmas **29**(11), 112708 (2022). https://doi.org/10.1063/5.0107534
Dimotakis, P.E.: The mixing transition in turbulent flows. J. Fluid Mech. **409**, 69–98 (2000)
Eça, L., Hoekstra, M.: A Procedure for the estimation of the numerical uncertainty of CFD calculations based on grid refinement studies. J. Comput. Phys. **262**, 104–130 (2014)
George, W.K., Davidson, L.: Role of initial conditions in establishing asymptotic flow behavior. AIAA J. **42**(3), 438–446 (2004)
Gittings, M., Weaver, R., Clover, M., Betlach, T., Byrne, N., Coker, R., Dendy, E., Hueckstaedt, R., New, K., Oakes, W.R., Ranta, D., Stefan, R.: The RAGE radiation-hydrodynamic code. Comput. Sci. Discov. **1**(1) (2008)
Grinstein, F.F.: Self-induced vortex ring dynamics in subsonic rectangular jets. Phys. Fluids **7**(10), 2519–2521 (1995)
Grinstein, F.F.: Vortex dynamics and entrainment in rectangular free jets. J. Fluid Mech. **437**, 69–101 (2001)
Grinstein, F.F.: Coarse grained simulation and turbulent mixing, 193–231. Cambridge University Press, Cambridge, United Kingdom (2016). Chap. 8
Grinstein, F.F.: Initial conditions and modeling for simulations of shock driven turbulent material mixing. Comput. Fluids **151**, 58–72 (2017)
Grinstein, F.F., Pereira, F.S.: Impact of numerical hydrodynamics in turbulent mixing transition simulations. Phys. Fluids **33**, 035126 (2021)
Grinstein, F.F., Wachtor, A.J.: Proof of concept: enslaved turbulent mixing. In: Grinstein, F.F. (ed.) Coarse grained simulations and turbulent mixing. Cambridge University Press, Cambridge, United Kingdom (2016). Chap. 1
Grinstein, F.F., Margolin, L.G., Rider, W.J.: Implicit large eddy simulations: computing turbulent flow dynamics, 1st edn. Cambridge University Press, New York, United States of America (2010)
Grinstein, F.F., Saenz, J.A., Dolence, J.C., Masser, T.O., Rauenzahn, R.M., Francois, M.M.: Effects of operator splitting and low mach-number correction in turbulent mixing transition simulations. Comput. Math. Appl. **78**(2), 437–458 (2019)
Grinstein, F.F., Chiravalle, V.P., Haines, B.M., Greene, R.K., Pereira, F.S.: Transition to turbulence in 3D ICF capsule implosions. International symposium on turbulence, heat and mass transfer, THMT-23, Rome, Italy, 11-15 September 2023, Begell House, Inc., Wallingford, UK, 10, 659–662 (2023)
Grinstein, F.F., Pereira, F.S., Rider, W.J.: Numerical approximations formulated as LES models. In: Moser, R. (ed.) Numerical methods in turbulence simulations. Elsevier, Academic Press, United Kingdom (2023). Chap. 10
Haan, S.W., Lindl, J.D., Callahan, D.A., al.: Point design targets, specifications, and requirements for the 2010 ignition campaign on the National Ignition Facility. Phys. Plasmas **18** (2011)
Hahn, M., Drikakis, D., Youngs, D.L., Williams, R.J.R.: Richtmyer–Meshkov turbulent mixing arising from an inclined material interface with realistic surface perturbations and reshocked flow. Phys. Fluids **23**, 046101 (2011)
Haines, B.M., Grinstein, F.F., Fincke, J.R.: Three-dimensional simulation strategy to determine the effects of turbulent mixing on inertial-confinement-fusion capsule performance. Phys. Rev. E **89**(5), 053302 (2014)
Haines, B.M., Vold, E.L., Molvig, K., Aldrich, C., Rauenzahn, R.: The effects of plasma diffusion and viscosity on turbulent instability growth. Phys. Plasmas **21**, 092306 (2014)
Haines, B.M., Grim, G.P., Fincke, J.R., Shah, R.C., Forrest, C.J., Silverstein, K., Marshall, F.J., Boswell, M., Fowler, M.M., Gore, R.A., Hayes-Sterbenz, A.C., Jungman, G., Klein, A., Rundberg, R.S., Steinkamp, M.J., Wilhelmy, J.B.: Detailed high-resolution three-dimensional simulations of OMEGA separated reactants ICF experiments. Phys. Plasmas **23** (2016)
Haines, B.M., Aldrich, C.H., Campbell, J.M., Rauenzahn, R.M., Wingate, C.A.: High-resolution modeling of indirectly driven high-convergence layered inertial confinement fusion capsule implosions. Phys. Plasmas **24**(5), 052701 (2017). https://doi.org/10.1063/1.4981222
Haines, B.M., Yi, S.A., Olson, R.E., Khan, S.F., Kyrala, G.A., Zylstra, A.B., Bradley, P.A., Peterson, R.R., Kline, J.L., Leeper, R.J., Shah, R.C.: The effects of convergence ratio on the implosion behavior of dt layered inertial confinement fusion capsules. Phys. Plasmas **24**(7), 072709 (2017). https://doi.org/10.1063/1.4993065
Haines, B.M., Olson, R.E., Sweet, W., Yi, S.A., Zylstra, A.B., Bradley, P.A., Elsner, F., Huang, H., Jimenez, R., Kline, J.L., Kong, C., Kyrala, G.A., Leeper, R.J., Paguio, R., Pajoom, S., Peterson, R.R., Ratledge, M., Rice, N.: Robustness to hydrodynamic instabilities in indirectly driven layered capsule implosions. Phys. Plasmas **26**(1), 012707 (2019). https://doi.org/10.1063/1.5080262

Haines, B.M., Clark, D.S., Weber, C.R., Edwards, M.J., Batha, S.H., Kline, J.L.: Cross-code comparison of the impact of the fill tube on high yield implosions on the Na-tional ignition facility. Phys. Plasmas **27**(8) (2020)

Haines, B.M., Shah, R.C., Smidt, J.M.: The rate of development of atomic mixing and temperature equilibration in inertial confinement fusion implosions. Phys. Plasmas **27**(10) (2020)

Haines, B.M., Shah, R.C., Smidt, J.M., Albright, B.J., Cardenas, T., Douglas, M.R., Forrest, C., Glebov, V.Y., Gunderson, M.A., Hamilton, C.E., Henderson, K.C., Kim, Y., Lee, M.N., Murphy, T.J., Oertel, J.A., Olson, R.E., Patterson, B.M., Randolph, R.B., Schmidt, D.W.: Observation of persistent species temperature separation in inertial confinement fusion mixtures. Nat. Commun. **11**, 544 (2020). https://doi.org/10.1038/s41467-020-14412-y

Haines, B.M., Keller, D.E., Long, K.P., McKay, M.D., Medin, Z.J., Park, H., Rauenzahn, R.M., Scott, H.A., Anderson, K.S., Collins, T.J.B., Green, L.M., Marozas, J.A., McKenty, P.W., Peterson, J.H., Vold, E.L., Di Stefano, C., Lester, R.S., Sauppe, J.P., Stark, D.J., Velechovsky, J.: The development of a high-resolution eulerian radiation-hydrodynamics simulation capability for laser-driven hohlraums. Phys. Plasmas **29**(8), 083901 (2022). https://doi.org/10.1063/5.0100985

Haines, B.M., Sauppe, J.P., Albright, B.J., Daughton, W.S., Finnegan, S.M., Kline, J.L., Smidt, J.M.: A mechanism for reduced compression in indirectly driven layered capsule implosions. Phys. Plasmas **29**(4), 042704 (2022). https://doi.org/10.1063/5.0083299

Hammel, B.A., Haan, S.W., Clark, D.S., Edwards, M.J., Langer, S.H., Marinak, M.M., Patel, M.V., Salmonson, J.D., Scott, H.A.: High-mode rayleigh-taylor growth in nif ignition capsules. High Energy Density Phys. **6**(2), 171–178 (2010). https://doi.org/10.1016/j.hedp.2009.12.005. ICHED 2009-2nd International Conference on High Energy Density Physics

Hussain, A.K.M.F., Husain, H.S.: Elliptic jets. Part I. characteristics of unexcited and excited jets. J. Fluid Mech. **208**, 257–320 (1989)

Jeong, J., Hussain, F.: On the identification of a vortex. J. Fluid Mech. **285**, 69–94 (1995)

LePape, S., Hopkins, L.F.B., Divol, L., Pak, A., Dewald, E.L., Bhandarkar, S., Bennedetti, L.R., Bunn, T., Biener, J., Crippen, J., Casey, D., Edgell, D., Fittinghoff, D.N., Gatu-Johnson, M., Goyon, C., Haan, S., Hatarik, R., Havre, M., Ho, D.D.-M., Izum, N., Jaquez, J., Khan, S.F., Kyrala, G.A., Ma, T., Mackinnon, A.J., MacPhee, A.G., MacGowan, B.J., Meezan, N.B., Milovich, J., Millot, M., Michel, P., Nagel, S.R., Nikroo, A., Patel, P., Ralph, J., Ross, J.S., Rice, N.G., Strozzi, D., Stadermann, M., Volegov, P., Yeamans, C., Weber, C., Wild, C., Callahan, D., Hurricane, O.A.: Fusion energy output greater than the kinetic energy of an imploding shell at the National ignition facility. Phys. Rev. Lett. **120**(24), 245003 (2018)

Leweke, T., Dizés, S.L., Williamson, C.H.K.: Dynamics and instabilities of vortex pairs. Annual Rev. Fluid Mech. **48**(1), 507–541 (2016)

Lindl, J.: Development of the indirect-drive approach to inertial confinement fusion and the target physics basis for ignition and gain. Phys. Plasmas **2**(11), 3933–4024 (1995). https://doi.org/10.1063/1.871025

Marinak, M.M., Kerbel, G.D., Gentile, N.A., Jones, O., Munro, D., Pollaine, S., Dittrich, T.R., Haan, S.W.: Three-dimensional HYDRA simulations of National ignition facility targets. Phys. Plasmas **8**, 2275–2280 (2001)

McNally, J.R., Rothe, K.E., Sharp, R.D.: Fusion re-activity graphs and tables for charged particle reactions. Technical report, Oak Ridge National Laboratory, Oak Ridge, TN, USA (1979)

Menikoff, R., Mjolsness, R.C., Sharp, D.H., Zemach, C.: Initial value problem for Rayleigh–Taylor instability of viscous fluids. Phys. Fluids **21**, 1674–1687 (1978)

Mihalas, D., Mihalas, B.W.: Foundations of radiation hydrodynamics. Courier Corporation, North Chelmsford, MA, USA (2013)

Mikaelian, K.O.: Effect of viscosity on Rayleigh–Taylor and Richtmyer–Meshkov instabilities. Phys. Rev. E **47**, 375 (1993)

Miller, S.C., Goncharov, V.N.: Instability seeding mechanisms due to internal defects in inertial confinement fusion targets. Phys. Plasmas **29**(8), 082701 (2022). https://doi.org/10.1063/5.0091949

Molvig, K., Simakov, A.N., Vold, E.L.: Classical transport equations for burning gas-metal plasmas. Phys. Plasmas **21** (2014)

Nuckolls, J., Wood, J., Thiessen, A., Zimmerman, G.: Laser compression of matter to super-high densities: thermonuclear (CTR) applications. Nature **239**, 139–142 (1972)

Pereira, F.S., Grinstein, F.F., Israel, D.M., Rauenzahn, R., Girimaji, S.S.: Modeling and simulation of transitional Rayleigh–Taylor flow with partially-averaged Navier–Stokes equations. Phys. Fluids **33**, 115118 (2021)

Pickworth, L.A., Hammel, B.A., Smalyuk, V.A., Robey, H.F., Benedetti, L.R., Hopkins, L.B., Bradley, D.K., Field, J.E., Haan, S.W., Hatarik, R., Hartouni, E., Izumi, N., Johnson, S., Khan, S., Lahmann, B., Landen, O.L., LePape, S., MacPhee, A.G., Meezan, N.B., Milovich, J., Nagel, S.R., Nikroo, A., Pak,

A.E., Petrasso, R., Remington, B.A., Rice, N.G., Springer, P.T., Stadermann, M., Widmann, K., Hsing, W.: Visualizing deceleration-phase instabilities in inertial confinement fusion implosions using an enhanced self-emission technique at the national ignition facility. Phys. Plasmas **25**(5), 054502 (2018). https://doi.org/10.1063/1.5025188

Pradeep, D.S., Hussain, F.: Core dynamics of a strained vortex: instability and transition. J. Fluid Mech. **447**, 247–285 (2001)

Ristorcelli, J.R., Gowardhan, A.A., Grinstein, F.F.: Two classes of Richtmyer-Meshkov instabilities: a detailed statistical look. Phys. Fluids **25**, 044106 (2013)

Robey, H.F., Boehly, T.R., Celliers, P.M., Eggert, J.H., Hicks, D., Smith, R.F., Collins, R., Bowers, M.W., Krauter, K.G., Datte, P.S., Munro, D.H., Milovich, J.L., Jones, O.S., Michel, P.A., Thomas, C.A., Olson, R.E., Pollaine, S., Town, R.P.J., Haan, S., Callahan, D., Clark, D., Edwards, J., Kline, J.L., Dixit, S., Schneider, M.B., Dewald, E.L., Widmann, K., Moody, J.D., Döppner, T., Radousky, H.B., Throop, A., Kalantar, D., DiNicola, P., Nikroo, A., Kroll, J.J., Hamza, A.V., Horner, J.B., Bhandarkar, S.D., Dzenitis, E., Alger, E., Giraldez, E., Castro, C., Moreno, K., Haynam, C., LaFortune, K.N., Widmayer, C., Shaw, M., Jancaitis, K., Parham, T., Holunga, D.M., Walters, C.F., Haid, B., Mapoles, E.R., Sater, J., Gibson, C.R., Malsbury, T., Fair, J., Trummer, D., Coffee, K.R., Burr, B., Berzins, L.V., Choate, C., Brereton, S.J., Azevedo, S., Chandrasekaran, H., Eder, D.C., Masters, N.D., Fisher, A.C., Sterne, P.A., Young, B.K., Landen, O.L., Van Wonterghem, B.M., MacGowan, B.J., Atherton, J., Lindl, J.D., Meyerhofer, D.D., Moses, E.: Shock timing experiments on the national ignition facility: initial results and comparison with simulation. Phys. Plasmas **19**(4), 042706 (2012). https://doi.org/10.1063/1.3694122

Robey, H.F., MacGowan, B.J., Landen, O.L., LaFortune, K.N., Widmayer, C., Celliers, P.M., Moody, J.D., Ross, J.S., Ralph, J., LePape, S., Berzak Hopkins, L.F., Spears, B.K., Haan, S.W., Clark, D., Lindl, J.D., Edwards, M.J.: The effect of laser pulse shape variations on the adiabat of nif capsule implosions. Phys. Plasmas **20**(5), 052707 (2013). https://doi.org/10.1063/1.4807331

Sagaut, P.: Large eddy simulation for incompressible flows. Springer, NY (2006)

Toro, E.F., Spruce, M., Speares, W.: Restoration of the contact surface in the HLL-Riemann solver. Shock Waves **4**(1), 25–34 (1994)

Vold, E.L., Rauenzahn, R.M., Aldrich, C.H., Molvig, K., Simakov, A.N., Haines, B.M.: Plasma transport in an eulerian AMR code. Phys. Plasmas **24** (2017)

Weber, C.R., Clark, D.S., Cook, A.W., Busby, L.E., Robey, H.F.: Inhibition of turbulence in inertial-confinement-fusion hot spots by viscous dissipation. Phys. Rev. E **89**, 053106 (2014)

Weber, C.R., Clark, D.S., Pak, A., Alfonso, N., Bachmann, B., Berzak Hopkins, L.F., Bunn, T., Crippen, J., Divol, L., Dittrich, T., Kritcher, A.L., Landen, O.L., Le Pape, S., MacPhee, A.G., Marley, E., Masse, L.P., Milovich, J.L., Nikroo, A., Patel, P.K., Pickworth, L.A., Rice, N., Smalyuk, V.A., Stadermann, M.: Mixing in icf implosions on the national ignition facility caused by the fill-tube. Phys. Plasmas **27**(3), 032703 (2020). https://doi.org/10.1063/1.5125599

Yao, J., Hussain, F.: Vortex reconnection and turbulence cascade. Annual Rev. Fluid Mech. **54**, 317–347 (2022)

Youngs, D.L., Williams, R.J.R.: Turbulent mixing in spherical implosions. Int. J. Numer Methods Fluids **56**, 1597–1603 (2008)

Zhou, Y.: Unification and extension of the similarity scaling criteria and mixing transition for studying astrophysics using high energy density laboratory experiments or numerical simulations. Phys. Plasmas **14**, 082701 (2007)

Zhou, Y.: Rayleigh–Taylor and Richtmyer–Meshkov instability induced flow, turbulence, and mixing. I. Phys. Rep. **720–722**, 1–136 (2017)

Zhou, Y.: Rayleigh–Taylor and Richtmyer–Meshkov instability induced flow, turbulence, and mixing. II. Phys. Rep. **723–725**, 1–160 (2017)